3D characterization of the structural transformation undergone by Cu@Ag core-shell nanoparticles following CO_2 reduction reaction

3D Characterization of the Structural Transformation Undergone by Cu@Ag Core-Shell Nanoparticles Following CO_2 Reduction Reaction.

Daniel Arenas Esteban[1,§], *Lien Pacquets*[1,2,§], *Daniel Choukroun*[2], *Saskia Hoekx*[1,2], *Ajinkya Anil Kadu*[1,3], *Jonathan Schalck*[2], *Nick Daems*[2], *Tom Breugelmans*[2,*], *Sara Bals*[1,*]

1 Electron Microscopy for Materials Science (EMAT), NANOlab Center of Excellence, University of Antwerp, 2020 Antwerp, Belgium.

2 Applied Electrochemistry and Catalysis (ELCAT), University of Antwerp, Universiteitsplein 1, 2610 Wilrijk, Belgium

3 Centrum Wiskunde & Informatica, Science Park 123, 1098 XG Amsterdam, The Netherlands.

§ These authors contributed equally to this work

* Corresponding Authors; E-mails: tom.breugelmans@uantwerpen.be, sara.bals@uantwerpen.be

Abstract

The increasing usage of metallic nanoparticles (NPs) is significantly advancing the field of electrocatalysis. In particular, Cu/Ag bimetallic interfaces are widely used to enhance the electrochemical CO_2 reduction reaction (eCO_2RR) towards CO and, more recently, C_2 products. However, drastic changes in the product distribution and performance when using Cu@Ag core-shell configurations can often be observed under electrochemical reaction conditions, especially during the first few minutes of the reaction. Possible structural changes that generate these observations remain underexplored; therefore, the structure-properties relationship is hardly understood. In this study, we use electron tomography to investigate the structural transformation mechanism of Cu@Ag core-shells NPs during the critical first minutes of the eCO_2RR. In this manner, we found that the crystallinity of the Cu seed determines whether the formation of a complete and homogeneous Ag shell is possible. Moreover, by tracking the particles' transformations, we conclude that the modifications of the Cu-Ag interface and Cu_2O enrichment at the surface of the NPs are key factors contributing to the product generation changes. These insights provide a better understanding of how bimetallic core-shell NPs transform under electrochemical conditions.

Introduction

Reducing CO_2 concentrations in the atmosphere has become an important priority to limit the detrimental effects of climate change. Among all developed strategies for CO_2 conversion, the electrochemical CO_2 reduction reaction (eCO_2RR) is considered one of the most sustainable and promising approaches[1] as it also allows for producing valuable chemical products such as multi-carbon alcohols or alkanes.[2,3] Although many metals have been tested, only Cu is capable of reducing CO_2 to hydrocarbons and alcohols by eCO_2RR due to its unique adsorption characteristics for intermediate products and its ability to realize C-C coupling reactions.[3,4] The

use of Cu as a catalyst allows for tuning the production towards certain chemical compounds through particle size,[5] the presence of certain facets,[6,7] and the incorporation of a second metal.[8] However, Cu NPs, unfortunately, degrade under eCO_2RR conditions, forming particle agglomerates. This is mainly driven by CO_2 adsorption and the negative potential generated on the surface.[9]

Combining Cu with a second metal can improve the catalytic activity and product selectivity,[10] therefore, employing core-shell Cu-based NPs can be a promising strategy to improve their performances. Cu-Ag bimetallic structures are currently widely used as catalysts for the production of C_2-products.[11–13] It has furthermore been observed that Cu@Ag core-shell NPs yield high faradaic efficiencies towards CO during the eCO_2RR.[14] The Cu@Ag core-shell configuration offers several advantages over pure Cu, including greater stability against oxidation and a catalytic tandem effect for the simultaneous production of C_{2+} products while reducing CO_2.[15,16] In addition, Cu@Ag core-shell NPs are more resource-efficient compared to monometallic Ag NPs as they require a reduced amount of Ag. Despite the large amount of prior work performed to improve the product selectivity and to boost the activity of Cu@Ag core-shell electrocatalysts, structural transformations that may occur during electrochemical operation remain poorly understood.[17] Such understanding is required to progress towards highly active, selective, and, most importantly, stable electrocatalysts. Focusing on the early stages of the eCO_2RR is particularly important in achieving this goal since the most significant differences in product concentration are usually observed in this short period.

Transmission electron microscopy (TEM) is an ideal technique to investigate the structure and composition of nanomaterials.[18] However, more than two-dimensional (2D) TEM images are often required to investigate the complete three-dimensional (3D) structure or composition of core-shell NPs. This limitation can be overcome by electron tomography. This technique uses

a tilt series of 2D projection images as an input for a reconstruction algorithm to obtain a 3D characterization of the structure of interest.[19,20] Currently, it is even possible to investigate the atomic structure of core-shell NPs in 3D, albeit for model-like systems.[21]

In this study, we investigated the early stages of the eCO_2RR of Cu@Ag core-shell NPs, focusing on the nanostructure transformation and its relationship with changes in product distribution. Chronopotentiometry experiments revealed that the product output shifts early in the reaction toward higher CO generation, whereas methane synthesis shifts to ethylene. Cyclic voltammetry in a three-electrode cell furthermore suggested crucial changes to the surface area accessible to the electrolyte as well as changes to the interface between Cu and Ag. To complement these measurements, we characterized the structure of these NPs by electron tomography with atomic resolution before and after applying an electric current. After careful investigation of the data, a sequential structure transformation pathway could be proposed, which is in good agreement with the changes in product generation observed by the electrochemical experiments, allowing for a coherent explanation for the increase in CO and ethylene production. Our study demonstrates that the polycrystalline nature of the Cu core in bimetallic Cu-Ag NPs results in anisotropic growth of the Ag shell and the formation of non-homogeneous shells with pinholes, compromising the structural stability of the NPs. During eCO_2RR, the Ag shell can be modified into more constrained shapes under electrochemical conditions by the adsorption of the generated CO molecules at the surface, which causes the enlargement of these pinholes and results in Cu leaching and fragmentation, ultimately leading to degradation of the NPs. This degradation can be inhibited by targeting monocrystalline Cu NPs and demands further investigation. Correlating the structural changes with the reaction products obtained provides a valuable tool for NP design that can direct the catalytic activity towards a specific desired product while enhancing the eCO_2RR.

Experimental section

Chemicals

Copper(II) acetate monohydrate (Cu(II)OAc, p.a., Janssen Chimica), Trioctylamine (TOA, 97%, Acros Organics), Tetradecylphosphonic acid (TDPA, 98%, Sigma Aldrich), Isoamyl ether (IAE, 99%, Sigma Aldrich), silver trifluoroacetate (Ag-TFA, 99.99%, trace metal basis, Sigma Aldrich), Ethanol (99.5% Extra Dry, AcrosSeal®, Acros Organics), iso-propanol (99.5%, AcrosSeal® Acros Organics), Potassium bicarbonate (Chem-Lab, 99,5%), Sigracet® 39BC (SGL Carbon) and Selemion® DSVN anion exchange membrane (AGC Engineering Co., Japan) were used during this research. All solutions were prepared with ultra-pure water (MQ, Milli-Q grade, 18.2 MΩcm).

Synthesis of Cu@Ag core-shell NPs

Sub-10 nm Cu@Ag core-shell NPs were successfully synthesized following a two steps procedure. Firstly, the Cu NPs were prepared using a modified synthesis based on the synthesis applied in Hung[16] and Osowiecki.[22] An air-free environment is essential to prevent the Cu NPs from oxidation. Prior to synthesis, the reaction solvent TOA was pre-dried with molecular sieves to reduce the water content. Subsequently, 122 mg of Cu(II)OAc was mixed with 82.3 mg TDPA in 10 mL of TOA and brought under an inert atmosphere using a Schlenk line by evacuating and refilling with Ar several times. This mixture was heated to 105 °C and retained for one hour while stirring. The solution was rapidly heated to 180 °C with an increment of ~3 °C min^{-1} and maintained for 30 min. After that, the temperature was further increased to 270 °C with the same increment and held for another 30 minutes. Eventually, the Cu NP mixture was cooled to room temperature and transferred under Ar to a glove box (Unilab Pro, MBraun) for particle purification. The as-prepared Cu NPs were purified by centrifuging a 1.25:1

mixture of 1:1 ethanol/iso-propanol and Cu suspension for 5-10 min at 5000 rpm. Subsequently, the precipitated Cu NPs were redispersed in hexane. This process was repeated three times, and the cleaned Cu NPs were eventually redispersed and stored in hexane. Before using the Cu NPs as a substrate for the synthesis of the Ag shell, they were redispersed in IAE, which served as the reaction solvent (Figure S1).

In a second step, Cu@Ag core-shell NPs were synthesized by two subsequent galvanic displacement steps where Ag atoms replaced Cu surface atoms. The Ag-TFA salt was dissolved in IAE (11 mg in 3 mL). The Ag-solution was slowly added to the Cu NPs suspension so that an Ag concentration of 40 at.% could be obtained each time. The reaction mixture was stirred for 2 hours at room temperature using a vortex and 2 hours at 90 °C while stirring for the first and second displacement steps, respectively. Afterward, the CuAg NCs were purified using the same cleaning method mentioned in the previous section. The CuAg NCs were eventually redispersed and stored in hexane.

Electrochemical investigation.

The eCO_2RR performance of Cu@Ag core-shell NPs was electrochemically evaluated by chronopotentiometry (CP) using a multi Autolab M204 potentiostat/galvanostat. Experiments were carried out in a three-compartment hybrid flow cell (as used by Choukroun et al.[23]) with 1 M $KHCO_3$ serving as the electrolyte in both anode and cathode compartments, which were separated by a Selemion® DSVN anion exchange membrane. The catholyte was recycled throughout the experiment at a flow rate of 0.2 mL min^{-1}. CO_2 was fed in flow-by mode at a flow rate of 7.5 sccm. The reactor outlet was connected in-line to a Thermo Trace 1300 gas chromatograph (GC) equipped with a TCD detector and a micropacked column (ShinCarbon ST 100/120, 2 m, 1 mm ID, Restek). Peak areas were converted to the corresponding

concentrations of H_2, CO, CH_4, and C_2H_4 based on calibration curves in the range of 0.1%-2%. The Faradaic efficiency (FE) was calculated using the following equation:

$$FE_i = \frac{j_i}{j_{tot}} = \frac{c_{i,t}\dot{V}P}{RT} \times \frac{n_i F}{j_{tot} A_{geo}}.$$

The molar flux (J_i) is calculated by assuming ideal gas behavior and plugging in the measured concentration ($c_{i,t}$) of product i in the gas phase stream, the outlet gas flow rate $\dot{V}$, and converting at standard temperature T, and pressure P. The associated current density is calculated using Faraday's law ($j_i = n_i F J_i / A_{geo}$) with j as the current density and A_{geo} as the exposed surface area (0.785 cm^2). The remaining constants are the gas constant (R=8.314 J mol^{-1} K^{-1}), Faraday's constant (F=96485 C mol^{-1}), and n_i, the number of transferred electrons for each product (2,2,8 and 12 for H_2, CO, CH_4 and C_2H_4, respectively).

After each injection into the GC, chronopotentiometry is stopped, and the system is left to relax to its open circuit potential (OCP) until completion of the GC run (15 min, including a cool-down period). Consequently, a constant current is again applied and maintained until the next sampling time. The working electrode (WE) consisted of a drop-cast Cu@Ag gas diffusion electrode (GDE) with a loading of 50 µg cm^{-2} used during the entire experiment. A leak-free Ag/AgCl electrode (W3-690053, Harvard Apparatus) and a carbon cloth served as a reference electrode (RE) and counter electrode (CE) in a three-electrode system, respectively. In the case of cyclic voltammetry experiments, the three-electrode system consisted of a glassy carbon (GC) with drop-cast Cu@Ag core-shell WE, a $Ag/AgCl_{sat}$ RE, and a carbon cloth CE. The potential was scanned at 100 mV s^{-1} between 0.21 V_{RHE} and 1.7 V_{RHE}, which comprises the different oxidation states of Cu and Ag in an Ar-saturated 0.1 M KOH solution at room temperature.

For the electrochemical experiments performed using the TEM grid, suspended NPs were drop-cast directly onto the carbon-coated side of the substrate inside a glove box to minimize air exposure. This allowed us to study the structural transformations of individual particles and self-assembled particle ensembles on a flat substrate, thereby eliminating the influence of surface roughness and sizeable interparticle spacing on particle reconstruction, agglomeration, and reaction performance. After the first characterization by TEM, The grids were transferred to the electrochemical H-type cell setup (Figure S2), where a charge of 70.6 mC (~ 2 mA cm^{-2}) was imposed onto the TEM grid for 2 minutes. Afterward, the TEM grid was washed with Milli Q, dried under Ar, and transferred to the electron microscope for further analysis. All potentials in this work are referenced to the reversible hydrogen electrode (RHE) using the equation below:

$$\boldsymbol{E_{RHE} = E_{measured} + 0.210V + 0.059 \cdot pH} - IR_u$$

where I is the measured current and R_u is the uncompensated resistance, which takes on different values depending on the electrolyte type, concentration, and exposed electrode area employed in each cell configuration.

Electron microscopy investigation.

High-Angle Annular Dark-Field Scanning Transmission Electron Microscopy (HAADF-STEM) and Energy Dispersive X-ray Spectroscopy (EDS) have been performed on an aberration-corrected cubed Thermofisher Titan microscope equipped with a Super-X EDS detector operating at 300 kV. EDS analyses were performed by acquiring at least 100 frames at a higher dosage of $2 \cdot 10^4$ e A^{-2} to ensure enough counts. Particle size distribution was performed by using ImageJ software applied to low-magnification HAADF images.

Electron tomography tilt series were acquired using a Fischione 2020 tomography holder. A high-resolution HAADF-STEM tilt series was acquired over a tilt range between ±75° with a tilt increment of 3°. In order to obtain atomic resolution in 3D and prevent possible particle alteration caused by electron beam damage, we employed a methodology based on rapid scanning. By acquiring HAADF-STEM projection images with short dwell times, we ensured the stability of the particle during electron beam exposure.[24] The projection images were acquired using five frames at 0.5 μs dwell time, while the image resolution was set to 2048x2048 pixels. Next, we used these images as input for a non-rigid registration method in combination with a convolutional neural network (CNN) which adequately corrects the distortions generated by fast scanning to obtain a clear atomic resolution image on each projection. The acquired series were aligned using cross-correlation, and 3D reconstructions were obtained using the Expectation Maximization (EM) algorithm, as implemented in Astra Toolbox.[25,26] In this study, the determination of the core-shell structure is of paramount importance. To achieve this, a semi-supervised learning algorithm[27] was utilized for the volumetric segmentation of Cu and Ag reconstructions. A rigorous manual segmentation process was initially conducted on 15 random slices from various 3D volumes obtained from the acquired data. These segmented slices were then utilized to train a deep convolutional neural network, specifically a U-Net architecture (encoder depth of 5, 64 number of filters, kernel size of 3 x 3, and stride of 1 in all convolution layers), for 100 epochs and a learning rate of 0.001. The trained U-Net was subsequently utilized to complete the segmentation of the volume. Precisely, the segmentations of orthoslices were estimated in all three directions, and a maximum strategy was employed to generate the final segmented volume.

Results and Discussion

Synthesis and electrochemical performance

The electrochemical CO_2 reduction reaction (eCO_2RR) catalytic performance of Cu@Ag core-shell NPs was evaluated by performing a chronopotentiometry experiment at 75 mA cm^{-2} for 600 s in a hybrid flow cell. A relatively small exposed GDE surface area (0.785 cm^2) and low NP loading were used as a compromise between experimental conditions which facilitate adequate mass transport of CO_2 and fast gas product detection on the one hand, and those encountered with TEM grids as electrode substrates on the other hand (see below). Figure 1 depicts the changes in the outlet gas-phase composition over time, whereas Figure S3 provides the corresponding FEs. The latter do not sum up to unity at the shortest sampling time (10 s) due to the incomplete saturation of the gas phase. Nevertheless, carbon monoxide and hydrogen are the major products. The aforementioned experimental design aspects (loading and surface area) also contribute to the high potentials observed after IR-drop correction in Figure 1.

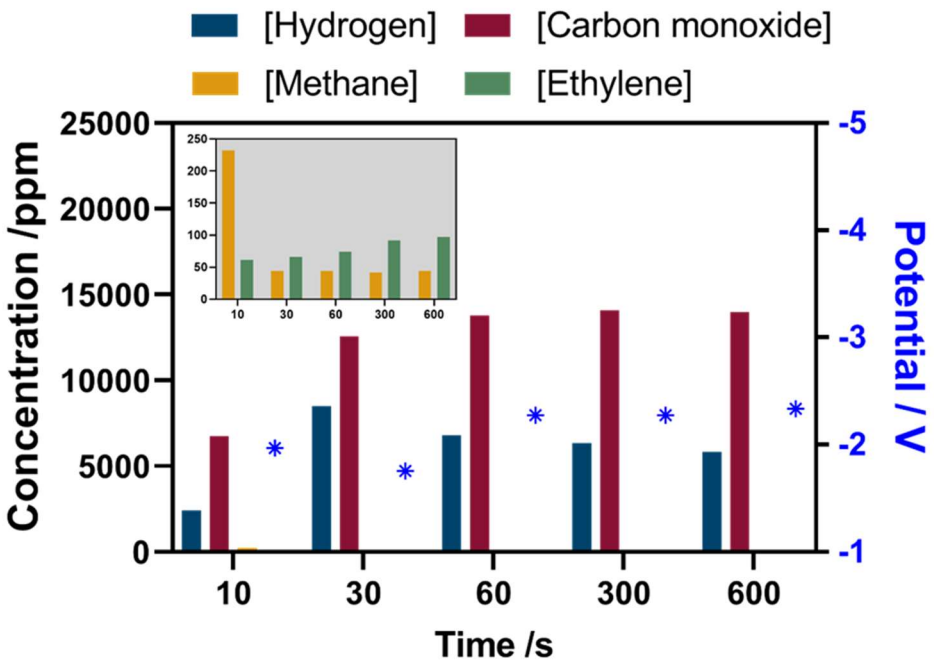

***Figure 1**: Evolution of the gas-phase selectivity of Cu@Ag core-shell NPs at 75 mA cm^{-2} during a 600 s experiment with gas-phase analysis at 10 s, 30 s, 60 s, 300 s, and 600 s. Substrate: Sigracet 39BC gas diffusion electrode. Experiments were performed in 1 M $KHCO_3$ with a CO_2 flow rate of 7.5 sccm and a catholyte recycle flow of 0.2 mL min^{-1}. Color bars show product distribution, whereas blue asterisks represent the potential measured at each time vs. RHE.*

After 60 seconds, CO concentrations practically double, and the production remains stable without any significant changes in potential after that (0.08 V_{RHE} difference). After tripling the initial concentration at 30 seconds, H_2 production gradually decays. This change in product distribution seems to indicate a nanostructural transformation of the core-shell NPs within the specified time window.[28] Cu@Ag core-shell NPs produce up to 232 ppm of methane within the first 10 s time window but only 44 ppm after 30 s. This is accompanied by a continuous increase in ethylene (along with CO) production throughout the rest of the experiment. In addition, the measured WE potential indicates a drastic change of 0.47 V_{RHE} in the 30 to 60 s time frame, reinforcing the hypothesis that a change in the morphology of the nanostructures has occurred, as was previously observed at longer reaction times towards either nanoclustering[9] or agglomeration.[29] The changes in product formation within different time frames may indicate that the transformation undergone by the Cu@Ag NPs involves several steps that do not

necessarily occur in sequential order. Note that the packing density and the loading of such NPs can influence the product distribution as well.[23]

To further investigate the structural evolution of Cu@Ag NPs and potentially link the impact of electrochemical rearrangement with core-shell structural changes, their behavior was further electrochemically analyzed by cyclic voltammetry (CV), represented in Figure 2a. During the first scan, a broad oxidation peak appeared between 1.13 V_{RHE} and 1.47 V_{RHE} (presented in Figure 2b), which seems to be stable over the rest of the performed cycles, and which can be associated with the formation of Cu^{+} and Cu^{2+}, as observed previously in sub-10 nm Cu@Ag core-shell NPs.[23] These observations indicate that the Cu surface is accessible from the beginning of the reaction, which may indicate that the Ag shell is not completely surrounding the Cu core. Regarding Ag, the anodic feature at 1.72 V_{RHE} and reduction shoulder around 1.65 V_{RHE} confirms its presence at the surface (Figure 2e). However, these peaks change with scan number, which can be attributed to surface changes.

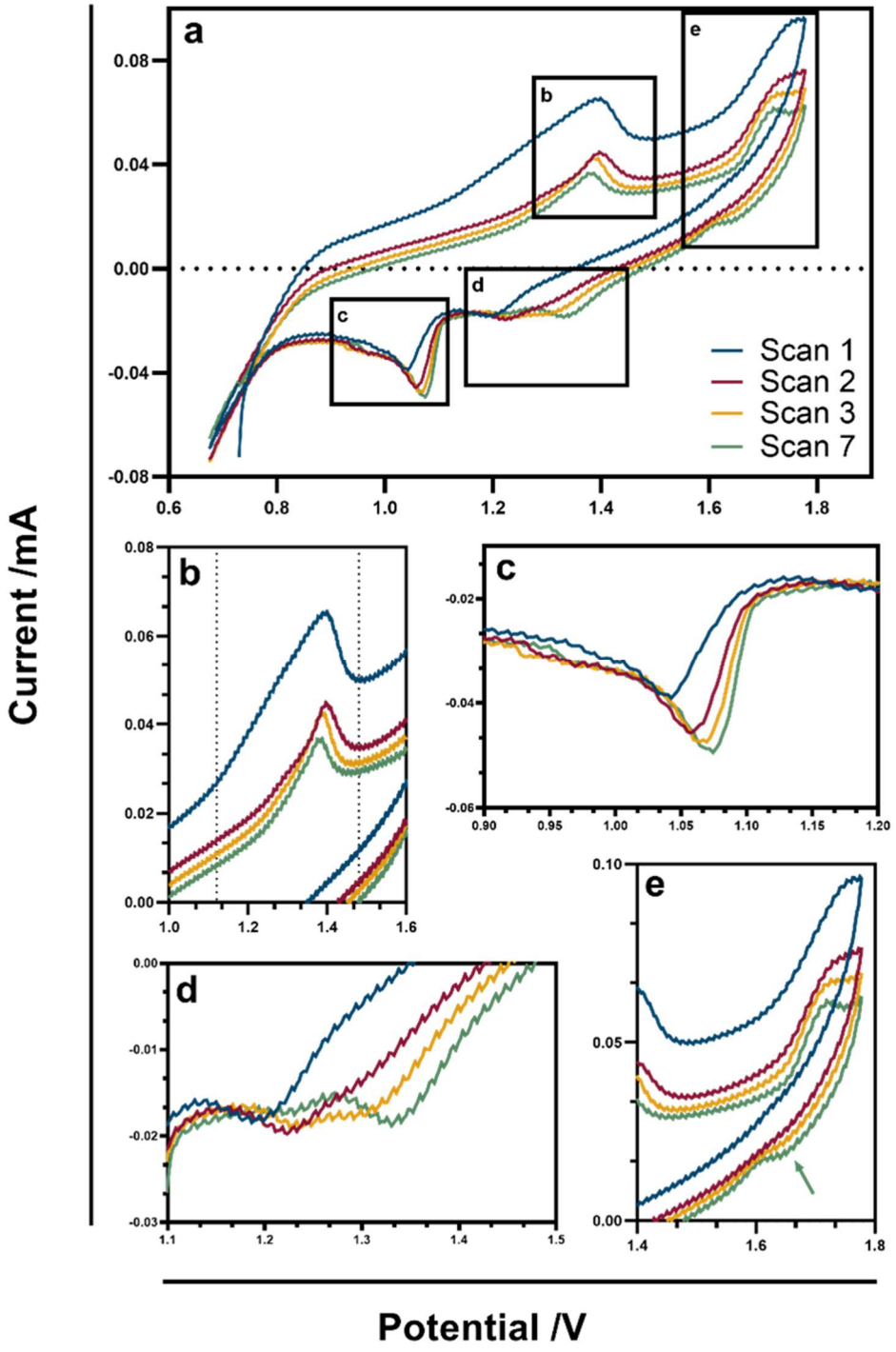

***Figure 2**: Cyclic voltammogram of Cu@Ag core-shell NPs (drop-cast on a glassy carbon electrode with a loading of 50 µg cm^{-2}) in Ar-saturated 0.1 M KOH at 100 mV s^{-1} within a range of 0.68 V_{RHE} to 1.78 V_{RHE} of the first (blue), second (red), third (orange) and seventh (green) scan (a). The oxidation of Cu (b), the reduction peaks of Cu (c, d), and the oxidation/reduction of Ag (e) are highlighted. The high signal-to-noise ratio can be attributed to the low NP concentration and, consequently, the low resulting currents.*

For the cathodic scan, the Cu reduction peak shifting from 1.04 to 1.07 V_{RHE} (highlighted in Figure 2c) was preceded by a smaller one also shifting from 1.17 to 1.33 V_{RHE} (presented in

Figure 2d) and respectively represents the reduction of the Cu^{+} to metallic Cu^{0} and Cu^{2+} to Cu^{+}. The intensity of the reduction peak starting at 1.17 V_{RHE} (Figure 2d) dropped between the first and second scans. From the third scan onwards, a cathodic shoulder is observed, and its intensity increases as the cycles progress. On the other hand, the reduction peak starting at 1.04 V_{RHE} increased in magnitude at higher scan numbers. These evolutions, including peak shifts and peak increments, can potentially be attributed to the rearrangements of the Cu^{+} surface[30] as well as Cu enrichment at the surface.[31] This clearly indicates that electrochemical rearrangement causes the Cu@Ag core-shell NPs structure to change. However, investigating structural details such as crystallinity and interface strain requires 3D characterization of these complex core-shell NPs, ideally at the atomic level.

Electron microscopy characterization

The core-shell NPs show a high degree of homogeneity in shape and size, as shown in Figure 3, corresponding to a low-magnification HAADF-STEM image. The particle size distribution, calculated by applying the Circular Hough Transform to the low magnification HAADF-STEM image in Figure 3a,[32] is presented as an inset. It shows an average particle size of 6.40 nm with a standard deviation of 1.46 nm (see Figure S4). The polydispersity ratio is 23%, which is relatively high. However, this is still desirable because the particles in the sample are more likely to have the same properties. EDS maps in Figure 3b show that most NPs yield a core-shell structure with an average composition of 40 at% and 60 at% of Ag and Cu, respectively. Bare Cu NPs are occasionally observed, such as the one highlighted with a dashed yellow circle in Figure 3b. The presence of these uncoated NPs adequately justifies the existence of the Cu oxidation/reduction peak observed in the first cycle during CV experiments presented previously (Figure 2). Interestingly, it can be observed that although a core-shell structure is

achieved, the Cu core is not always centered in the particle, but the Ag shell forms a heterogeneous layer. This deviation is likely attributed to the formation of a crescent-shaped Ag coating on the Cu NPs, prior to complete coverage.[22] The high-resolution HAADF-STEM image presented in Figure 3c reveals that both the Cu core and Ag shell exhibit polycrystalline characteristics since the growth of Ag follows the crystal direction of Cu, which is confirmed by the Fast Fourier Transform (FFT) taken from the region marked by a yellow square. The polycrystalline nature of the Cu NPs induces the same crystal configuration on the Ag shell, leading to a heterogeneous growth and a non-uniform thickness, as shown by the yellow arrows in Figure 3c, where some parts of a shell with a thickness of 3 nm versus 1 nm.

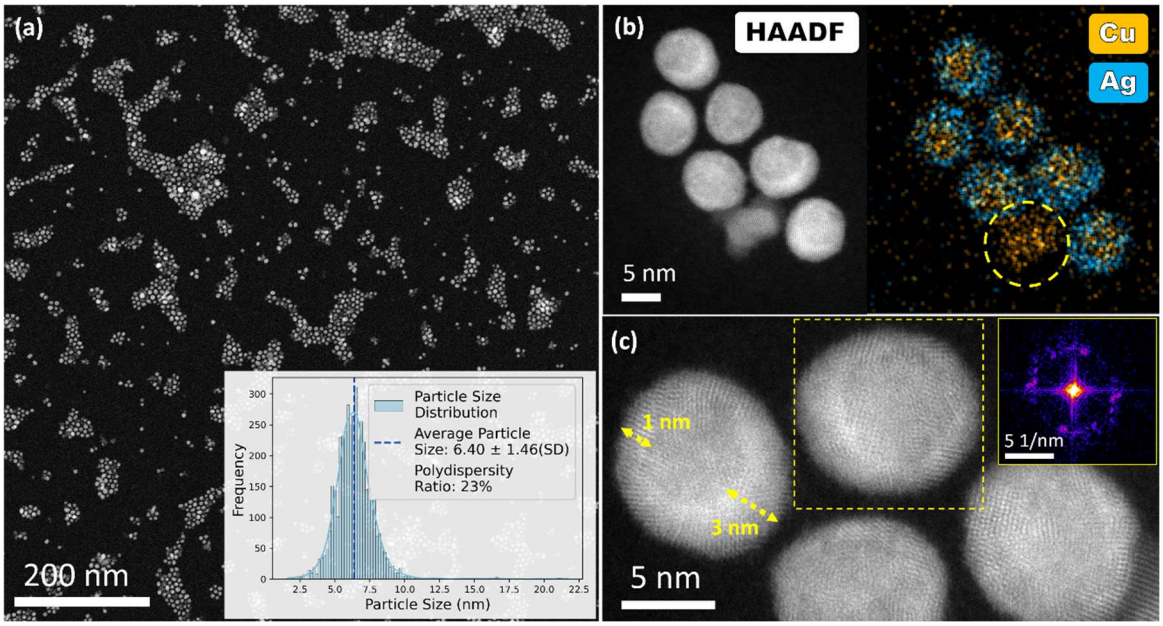

***Figure 3**: Low magnification HAADF-STEM image of the Cu@Ag NPs and particle size distribution (a). EDS analysis performed on several Cu@Ag NPs demonstrating its core-shell elemental distribution (b). Atomic resolution HAADF-STEM image where the uneven and polycrystalline Ag shell can be visualized (c), with an inset FFT acquired for the NP marked by a yellow square.*

Since 2D images are insufficient to demonstrate the complete formation of the core-shell structure, electron tomography in HAADF-STEM mode was performed. 3D visualizations of two NPs with a partial and an apparently complete Ag shell are presented in Figure 4a and Supporting Movie S1. These results show that not all particles are completely coated, and the non-uniformity of the Ag shell leads to an overall oblate morphology of the entire core-shell

NPs. Furthermore, we observed that even the NPs with apparently full Ag coverage have atomic-sized pin holes that expose the core to the outside, as highlighted in Figure 4a by a white dashed circle. This incomplete and heterogeneous Ag coverage of Cu NPs was already predicted by the nano-crescent growing model commented on above[22] as well as theoretical studies that indicated that the formation of a perfect core-shell structure for similar size NPs based on these two metals is not energetically favorable.[22] From orthoslices taken through the 3D reconstruction of one of the Cu@Ag NPs, the atomic lattice of the core and shell could be visualized. In this manner, we could reveal several crystal defects in the Cu core's interior, such as twin planes and edge dislocations (Figure 4b and c, respectively). It can be expected that these defects are strongly connected to the polycrystalline character of the Ag shell. From one of the orthoslices, an intensity line profile across the Ag-Cu interface was acquired, as illustrated in Figure 4d. For uncoated Cu, oxidation is likely to occur during exposure to air. The (111) interplanar distances of CuO, as well as Cu2O (i.e., 0.25 nm, C2/c, and 0.24 nm Pn-3m, respectively), are both close to those of Ag (i.e., 0.24 nm, Fm-3m). However, from Figure 4d, a (111) interplanar distance was observed corresponding to the expected distance for metallic Cu (i.e., 0.20 nm, Fm-3m). These observations suggest that the presence of the pinholes is insufficient to oxidize the core of the pristine Cu@Ag NPs.

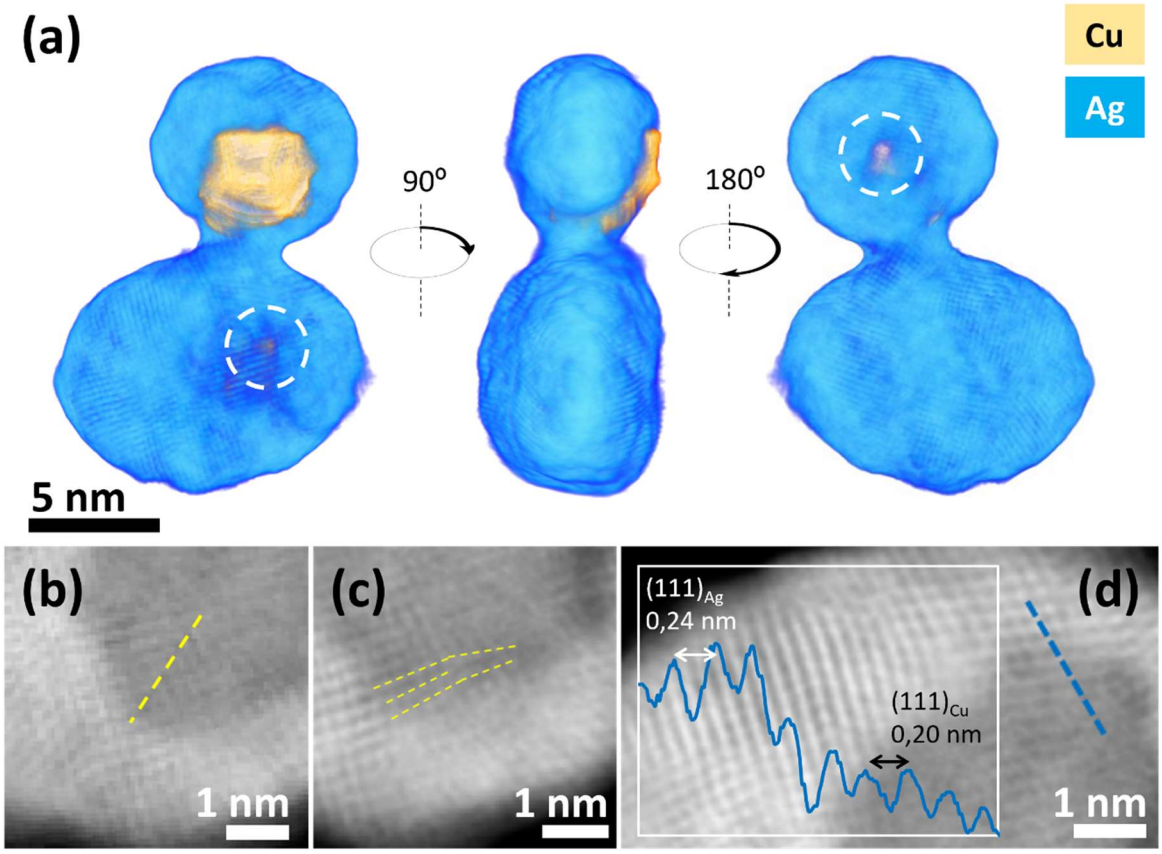

***Figure 4**: 3D visualizations of an electron tomography reconstruction of two connected Cu@Ag core-shell NPs imaged along different viewing directions (a). Orthoslices through the 3D reconstruction reveal the presence of defects such as twin planes (b) or edge dislocations (c) in the Cu core. An intensity line scan acquired from an orthoslice across the core-shell interface shows different distances along the (111) direction corresponding to the fcc crystal structure of Ag and Cu, respectively (d). Orthoslices were obtained from magnified areas of the reconstruction (Figure S5) as indicated by yellow, green, and red rectangles.*

Structural transformations of Cu@Ag core-shell NPs under CO_2 operating conditions

To investigate the dynamic evolution of the Cu@Ag core-shell nanostructure during electrocatalysis, an electrochemical batch setup (Figure S2) was utilized to apply a total charge of 70.6 mC (approximately 2 mA cm^{-2}) directly to the TEM grid used for characterization in Figure 3 and Figure 4. Given the inherent challenges associated with tracking temporal changes when the transformation time is indistinguishable and occurs concurrently, this study examines the diverse shapes encountered and establishes a logical correlation among them to propose a plausible transformation pathway, aligning with the initial expectations. Due to limitations in

the maximum electrical charge that a TEM grid can support, the applied current density was substantially lower than the value used in a standard chronopotentiometry experiment (75 mA cm^{-2}), where the NPs were deposited onto a GDE to serve as the working electrode in the flow cell. However, images of the NPs used for the standard chronopotentiometry experiments performed at different times and collected by electrode surface scraping do not show apparent differences from other experimental times as well as similar NP transformation features in all the cases, revealing that the results could be extrapolated (Figure S6). The low magnification HAADF-STEM image in Figure 5a, obtained from the sample after electrochemical experiments, reveals a higher degree of agglomeration between NPs than their initial appearance in Figure 3. Higher magnification HAADF-STEM imaging revealed diverse nanostructures coexisting within the same sample, indicating an unsynchronized nanostructure transformation. Control experiments were performed by exposing the particles to air, electrolyte, and even current in the absence of CO2 to ensure that the observed transformations occur due to the eCO_2RR. The core-shell structures were observed to maintain good stability under these conditions (Figures S7 and S8). A first observation is illustrated in Figure 5b, showing that Cu leached out from the original core-shell nanostructures (marked by a yellow arrow), forms a Janus-type particle (highlighted by a green arrow), and sometimes even separates from the core-shell structure to form smaller NPs as can be observed on the bottom part of Figure 5c. On the other hand, the Ag parts of the Janus-type particles exhibit a tendency to aggregate, as can be observed in Figures 5c and 5d (indicated by blue dashed circles). Moreover, for some structures, the EDS data in Figure 5d demonstrate an apparent inversion of the core-shell elemental distribution, possibly due to two aggregated Janus-type structures.

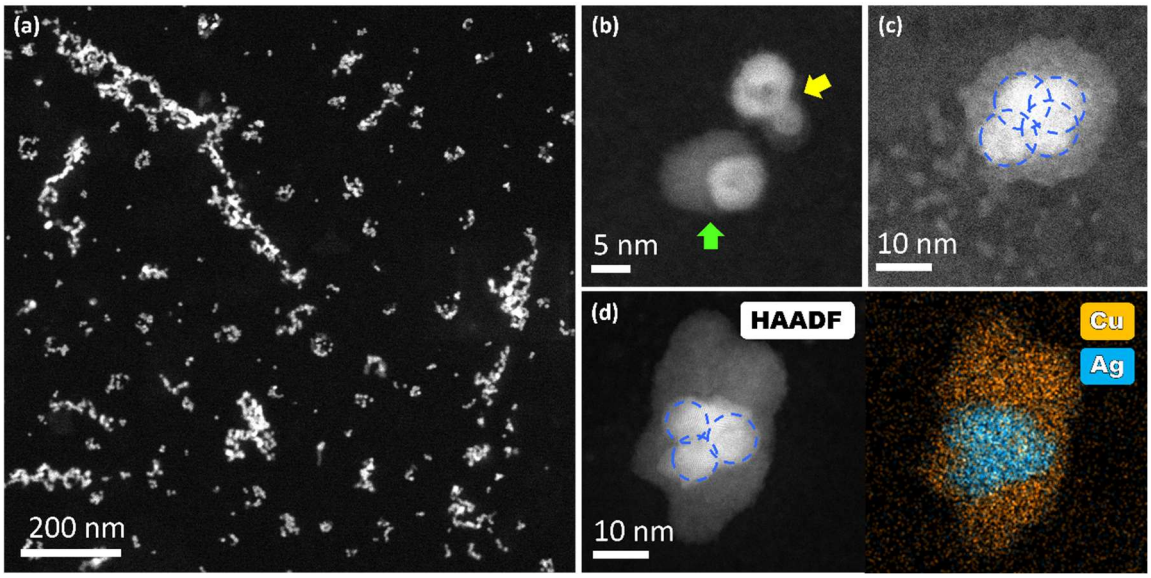

***Figure 5**: Low magnification HAADF-STEM image and particle size distribution analysis of the Cu@Ag NPs from Figure 1 after exposure to a total charge of 70.6 mC (a). High-resolution detail of the NPs showing Cu leaching and Janus-type structure formation indicated by yellow and green arrows, respectively (b). High-resolution image of an agglomeration of Janus particles (c). EDS analysis was performed on one of the structures where the elementary distribution in the core-shell seems to be inverted, identifying the Cu as the low-intensity material in the HAADF-STEM image (d).*

To obtain further insights, we again performed atomic resolution electron tomography for representative examples of the different observed NP structures. The results are presented in Figure 6 and Supporting Movie S2. Starting from the previously characterized Cu@Ag NP with an apparently complete core-shell structure illustrated in Figure 4 (Figure 6a, before the current application), a transformation process has been extrapolated using the different types of transformed nanostructures found on the TEM grid. The process appears to begin with the leaching of Cu from the core of the NP, likely through atomic-sized pinholes in the Ag shell. Notably, unmodified core-shell particles with these small pinholes were also observed (Figure S9), suggesting that more than their mere presence is required for Cu leaching. However, it is hypothesized that the Ag shell undergoes modifications in the presence of CO_2 under the influence of electrochemical charging, leading to the formation of more confined structures. [33] Consequently, this phenomenon promotes the enlargement of pinholes. It facilitates the adsorption of both CO_2 and reaction by-products onto the Cu surface, causing sufficient

mobility for surface atoms to displace towards the Ag surface and ultimately resulting in Cu leaching.[22] This effect can be confirmed when analyzing the Cu trace found connecting the remaining Cu in the core, and that of the surface in the transient form between the core-shell and Janus structures in Figure 6b further explains the origin of the copper at the surface. The diffusion of Cu from the core to the surface reshapes the original core-shell structure into a Janus particle. At the same time, Ag begins to rearrange into a solid particle, filling the space created by the leached Cu and potentially representing an extra driving force for completely displacing the remaining Cu on the core (Figure 6b). Additionally, Cu oxidizes to Cu_2O upon exposure to the surface, as evidenced by crystallographic analysis in the Supporting Information (Figure S9). In some cases, the transformation progresses toward a complete Cu covering of the freshly formed solid Ag NP in a new, completely inverted Ag@Cu_2O core-shell structure (Figure 6c). Recent operando TEM studies have demonstrated that these Ag@Cu_2O core-shell structures are unstable during eCO_2RR, leading to Cu fragmentation on the surface and Ag agglomerations.[34] Subsequently, this step can be linked with previous observations of the fragmentation process from the image in Figure 5c. A final step of the transformation pathway indicates that the process does not occur in a synchronized manner. Figure 6d shows a bigger NP, which is likely formed by the agglomeration of a single Ag solid particle with three Cu@Ag core-shell NPs, as well as a separated intermediate Cu-Ag Janus particle at the bottom. The final step of the analysis revealed evidence of sintering of NP, not only from solid Ag NPs but also from all the different configurations. This step highlights the interaction between all the shapes observed in the sample. It elucidates that the changes elicited in the eCO_2RR product distribution cannot be solely attributed to isolated events in the transformation process but rather stem from a combination of these morphological factors.

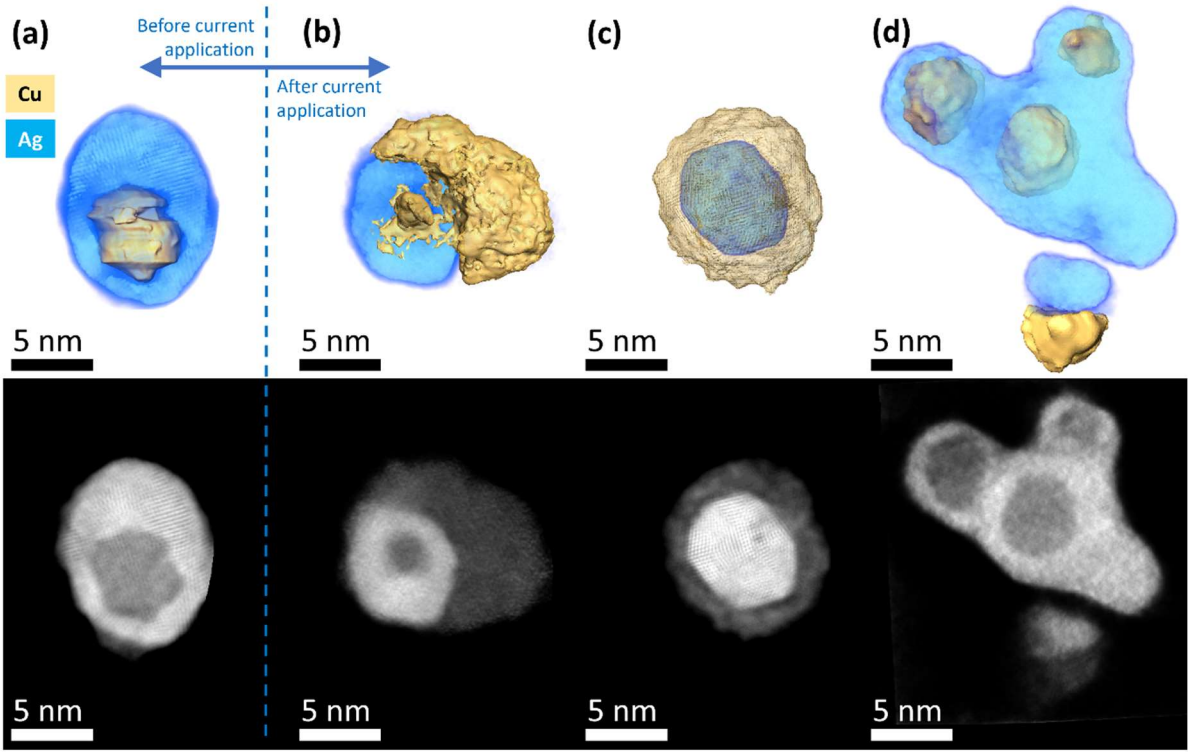

***Figure 6**: 3D reconstructions and their respective orthoslices for the Cu@Ag NPs' proposed transformation mechanism before (a) and after (b, c, d) current application.*

The discussion conversion pathway for Cu@Ag core-shell NPs proposed above seems to be in agreement with the electrocatalytic experiments. The factor triggering the transformation of the NPs is the crystallinity of the Cu core NP. The polycrystallinity of these pristine NPs generates a heterogeneous growth of the Ag coating, resulting in a defeated layer where pinholes can be observed, exposing the nucleus to the outside. In an attempt to achieve complete coverage, we performed a further experiment increasing the Ag concentration by 5%, but this led to an increased yield of Janus structures rather than complete core-shell structures. (Figure S10). However, we also observed a Cu@Ag core-shell NP with an apparently monocrystalline structure and homogeneous coverage after equivalent electrochemical testing. This observation was further confirmed by atomic resolution electron tomography, which revealed a fully covered and monocrystalline Ag shell capable of protecting the metallic Cu NP (Figure S11).

This observation supports our message that the crystal structure plays a crucial role in NP stability and indicates that achieving homogeneous coverage is possible if the monocrystalline of the pristine Cu NPs can be controlled. Consequently, the transformation of Cu@Ag core-shell NPs occurred in two stages. The first stage is characterized by Cu leaching from the core-shell through pinholes in the Ag shell. Recent studies showed CO adsorption as the critical factor in destabilizing general Cu surfaces.[35–37] Since the formation of a complete homogeneous Ag shell is not energetically stable, CO molecules (generated on the Ag shell) can be expected to be directly responsible for generating the necessary electrochemical driving force to reshape the Ag shell, increasing the pinhole sizes. Figure S8 provides empirical evidence supporting the proposition, as it demonstrates the continued stability of the core-shell structures in the absence of CO_2 when subjected to an applied electric current. This facilitates the diffusion of CO molecules to the Cu surface, where the negative Cu-CO interface energy (large energy of adsorption) represents a strong driving force toward Cu leaching. Once Cu reaches the surface, it readily oxidizes into Cu_2O.[9] The second stage of the transformation corresponds to the sintering and agglomeration of the Ag. Such a two-step process has recently been observed for CuZn NPs under similar eCO_2RR reaction conditions.[38]

This two-step conversion mechanism could potentially be the leading cause for the changes observed during the chronopotentiometry (Figure 1) and the CV (Figure 2) experiments. The ethylene production, present from the beginning of the synthesis process, most likely from accessible uncoated Cu surfaces, increased along the course of the experiment due to the increased availability of Cu surface, which is crucial for the C-C coupling.[16,39] The rapid decrease in methane production can be related to changes in the accessible surface Ag/Cu ratio along the experiment. During the first stages of the experiment, the Ag/Cu ratio decreases rapidly due to the leaching of Cu to the surface, increasing its share at the surface. Recent research showed that increasing the surface concentration of Cu in bimetallic Cu-Ag alloys, as

well as Cu-Au NPs, suppressed methane formation.[23,28] Note that the changes in methane production can also be attributed to the availability of CO at the electrocatalyst surface, as it is observed that the increase in CO production after 10 s led to the drop in methane production. CO is not only the main product obtained during the reaction from the beginning of the experiment, but its production clearly benefits from the structural transformations that the NPs undergo, reaching a stable value after 300 sec, which could potentially be explained by the already good performance of monometallic Ag catalysts towards CO. This will ensure the CO production after the occurrence of structural conversion at the early stages of the CO_2 reduction process. However, if Ag continues its aggregating trend in further steps of the reaction, a decrease in the total accessible surface area will occur and, therefore, a drop in CO production. Since it has been observed that the structural transformations occur gradually, it can be deduced that it is the combination of all of the marked forms which enhances the total CO production.

Conclusions

In this study, EDS analysis and high-resolution electron tomography were utilized to expose that Cu@Ag core-shell NPs, previously thought to have a largely spherical and fully covered Ag shell, are actually oblate and not homogeneously covered by Ag, with even atomic-sized pinholes that expose the Cu core to the surface. A transformation pathway has been hypothesized based on the 3D characterization of the different nanostructures found after the current application. These studies revealed that the enlargement of the Ag shell pinholes through electrochemical rearrangement is the leading cause of Cu leaching and the subsequent structural transformations of the NPs. Cu leaching caused an increase in ethylene production and a decrease in methane production, both effects originating from the changing Cu/Ag interface and Cu enrichment at the surface. Remarkably, the transformed Cu-Ag core-shell structure practically doubles the production of CO, probably due to the combined effect of the

different structures adopted since the structure transformation does not occur simultaneously. By combining electrochemistry and advanced electron microscopy techniques, we were able to obtain a better understanding of the evolution of the structure-properties relationship of these Cu@Ag core-shell NPs and their effect on the electrocatalytic performance, which in the specific case studied in this work, can be interpreted as a rapid catalyst activation process for CO production at the early stages of the eCO_2RR. These findings significantly contribute to the current understanding of morphological transformations in not only Cu@Ag core-shell configurations but also in other largely immiscible metal combinations. Future studies on the synthesis of monocrystalline metal cores may enhance the stability of core-shell NPs, as it has been established that the crystallinity of the central metal NP is a crucial factor for the formation of a complete and homogeneous second metal shell. The access to the surface of the inner metal can represent an essential driving force toward structural reconfiguration. Furthermore, it is important to note that even with a well-preserved nanostructure, particles can still exhibit agglomeration tendencies, emphasizing the potential benefit of utilizing a highly porous matrix in future studies.

ASSOCIATED CONTENT

The Supporting Information is available free of charge via the Internet at http://pubs.acs.org. Additional experimental details: HAADF-STEM image of monodisperse sub-10 nm Cu NPs, Electrochemical batch set-up, Faradaic Efficiencies (FE), Cu@Ag NPs particle size distribution, 3D visualizations and orthoslices performed, HAADF-STEM images of Cu@Ag core-shell NPs after chronopotentiometry experiment over carbon support, HAADF-STEM images of air exposure control experiment, HAADF-STEM images of electrolyte exposure control experiment, HAADF-HRSTEM image projection of Cu leaching, Cu@Ag core-shell NP synthesized with an increase in Ag concentration of 5%, Complete Cu@Ag core-shell NP

after the electrochemical experiment. (DOC); Support movie Movie_S1_Cu@AgNPs (MP4); Support movie Movie_S2_transformation (MP4).

AUTHOR INFORMATION

Corresponding author

Tom Breugelmans – Applied Electrochemistry and Catalysis (ELCAT), University of Antwerp, Universiteitsplein 1, 2610 Wilrijk, Belgium. Email: tom.breugelmans@uantwerpen.be

Sara Bals – Electron Microscopy for Materials Science (EMAT), NANOlab Center of Excellence, University of Antwerp, 2020 Antwerp, Belgium. Email: sara.bals@uantwerpen.be

Authors

Daniel Arenas Esteban – Electron Microscopy for Materials Science (EMAT), NANOlab Center of Excellence, University of Antwerp, 2020 Antwerp, Belgium.

Lien Pacquets – Electron Microscopy for Materials Science (EMAT), NANOlab Center of Excellence, University of Antwerp, 2020 Antwerp, Belgium. Applied Electrochemistry and Catalysis (ELCAT), University of Antwerp, Universiteitsplein 1, 2610 Wilrijk, Belgium.

Daniel Choukroun – Applied Electrochemistry and Catalysis (ELCAT), University of Antwerp, Universiteitsplein 1, 2610 Wilrijk, Belgium.

Saskia Hoekx – Electron Microscopy for Materials Science (EMAT), NANOlab Center of Excellence, University of Antwerp, 2020 Antwerp, Belgium. Applied Electrochemistry and Catalysis (ELCAT), University of Antwerp, Universiteitsplein 1, 2610 Wilrijk, Belgium.

Ajinkya Kadu – Electron Microscopy for Materials Science (EMAT), NANOlab Center of Excellence, University of Antwerp, 2020 Antwerp, Belgium. Centrum Wiskunde & Informatica, Science Park 123, 1098 XG Amsterdam, The Netherlands.

Jonathan Schalck – Applied Electrochemistry and Catalysis (ELCAT), University of Antwerp, Universiteitsplein 1, 2610 Wilrijk, Belgium.

Nick Daems – Applied Electrochemistry and Catalysis (ELCAT), University of Antwerp, Universiteitsplein 1, 2610 Wilrijk, Belgium.

ORCID

Daniel A. Esteban: 0000-0002-5626-9848

Lien Pacquets: 0000-0001-9457-685X

Daniel Choukroun: 0000-0002-3047-2506

Saskia Hoekx: 0000-0003-3107-6473

Ajinkya A.Kadu: 0000-0003-0853-1378

Jonathan Schalck: 0000-0003-4118-0266

Nick Daems: 0000-0001-7230-8950

Tom Breugelmans: 0000-0001-5538-0408

Sara Bals: 0000-0002-4249-8017

Author Contributions

D.A.E. wrote the manuscript and performed the electron microscopic analysis. L.P. wrote the manuscript and performed the synthesis Cu@Ag core-shell NPs and the electrochemical CP and CV measurements. D.C. performed the synthesis and design flow set-up. S.H. performed

the TEM analysis of the Cu NPs. A.A.K. develop the neural network-based approach for particle segmentation. J.S. designed the batch set-up. N.D., S.B., and T.B. conceived the idea and supervised the project

Acknowledgments

L.P. was supported through a PhD fellowship strategic basic research (1S56920N) of the Research Foundation – Flanders (FWO). S.H. was supported through a PhD fellowship strategic basic research (1S42621N) of the Research Foundation – Flanders (FWO). S.B., D.A.E., and A.A.K. acknowledge financial support from ERC Consolidator Grant Number 815128 REALNANO. This research was financed by the research council of the University of Antwerp (BOF-GOA 33928).

Notes

The authors declare no competing financial interest.

References

(1) Garg, S.; Li, M.; Weber, A. Z.; Ge, L.; Li, L.; Rudolph, V.; Wang, G.; Rufford, T. E. Advances and Challenges in Electrochemical CO2 Reduction Processes: An Engineering and Design Perspective Looking beyond New Catalyst Materials. *Journal of Materials Chemistry A*. Royal Society of Chemistry January 28, 2020, pp 1511–1544. https://doi.org/10.1039/c9ta13298h.

(2) Jaster, T.; Gawel, A.; Siegmund, D.; Holzmann, J.; Lohmann, H.; Klemm, E.; Apfel, U. P. Electrochemical CO2 Reduction toward Multicarbon Alcohols - The Microscopic World of Catalysts & Process Conditions. *iScience*. Elsevier Inc. April 15, 2022, p 104010. https://doi.org/10.1016/j.isci.2022.104010.

(3) Pei, Y.; Zhong, H.; Jin, F. A Brief Review of Electrocatalytic Reduction of CO_2 —Materials, Reaction Conditions, and Devices. *Energy Sci Eng* **2021**, *9* (7), 1012–1032. https://doi.org/10.1002/ese3.935.

(4) Nitopi, S.; Bertheussen, E.; Scott, S. B.; Liu, X.; Engstfeld, A. K.; Horch, S.; Seger, B.; Stephens, I. E. L.; Chan, K.; Hahn, C.; Nørskov, J. K.; Jaramillo, T. F.; Chorkendorff, I. Progress and Perspectives of Electrochemical CO2 Reduction on Copper in Aqueous Electrolyte. *Chemical Reviews*. American Chemical Society June 26, 2019, pp 7610–7672. https://doi.org/10.1021/acs.chemrev.8b00705.

(5) Iyengar, P.; Huang, J.; de Gregorio, G. L.; Gadiyar, C.; Buonsanti, R. Size Dependent Selectivity of Cu Nano-Octahedra Catalysts for the Electrochemical Reduction of CO2 to CH4. *Chemical Communications* **2019**, *55* (60), 8796–8799. https://doi.org/10.1039/c9cc02522g.

(6) Arán-Ais, R. M.; Scholten, F.; Kunze, S.; Rizo, R.; Roldan Cuenya, B. The Role of in Situ Generated Morphological Motifs and Cu(i) Species in C2+ Product Selectivity during CO2 Pulsed Electroreduction. *Nat Energy* **2020**, *5* (4), 317–325. https://doi.org/10.1038/s41560-020-0594-9.

(7) de Gregorio, G. L.; Burdyny, T.; Loiudice, A.; Iyengar, P.; Smith, W. A.; Buonsanti, R. Facet-Dependent Selectivity of Cu Catalysts in Electrochemical CO2 Reduction at Commercially Viable Current Densities. *ACS Catal* **2020**, *10* (9), 4854–4862. https://doi.org/10.1021/acscatal.0c00297.

(8) Gustavsen, K. R.; Wang, K. Recent Advances on Enhancing the Multicarbon Selectivity of Nanostructured Cu-Based Catalysts. *Physical Chemistry Chemical Physics*. Royal Society of Chemistry June 14, 2021, pp 12514–12532. https://doi.org/10.1039/d1cp00908g.

(9) Huang, J.; Hörmann, N.; Oveisi, E.; Loiudice, A.; De Gregorio, G. L.; Andreussi, O.; Marzari, N.; Buonsanti, R. Potential-Induced Nanoclustering of Metallic Catalysts during Electrochemical CO2 Reduction. *Nat Commun* **2018**, *9* (1), 1–9. https://doi.org/10.1038/s41467-018-05544-3.

(10) Wang, X.; Chen, Q.; Zhou, Y.; Li, H.; Fu, J.; Liu, M. Cu-Based Bimetallic Catalysts for CO2 Reduction Reaction. *Advanced Sensor and Energy Materials* **2022**, *1* (3), 100023. https://doi.org/10.1016/j.asems.2022.100023.

(11) Kuhn, A. N.; Zhao, H.; Nwabara, U. O.; Lu, X.; Liu, M.; Pan, Y.; Zhu, W.; Kenis, P. J. A.; Yang, H. Engineering Silver-Enriched Copper Core-Shell Electrocatalysts to Enhance the Production of Ethylene and C_{2+} Chemicals from Carbon Dioxide at Low Cell Potentials. *Adv Funct Mater* **2021**, *31* (26), 2101668. https://doi.org/10.1002/adfm.202101668.

(12) Hoang, T. T. H.; Verma, S.; Ma, S.; Fister, T. T.; Timoshenko, J.; Frenkel, A. I.; Kenis, P. J. A.; Gewirth, A. A. Nanoporous Copper-Silver Alloys by Additive-Controlled Electrodeposition for the Selective Electroreduction of CO2 to Ethylene and Ethanol. *J Am Chem Soc* **2018**, *140* (17), 5791–5797. https://doi.org/10.1021/jacs.8b01868.

(13) Chen, C.; Li, Y.; Yu, S.; Louisia, S.; Jin, J.; Li, M.; Ross, M. B.; Yang, P. Cu-Ag Tandem Catalysts for High-Rate CO2 Electrolysis toward Multicarbons. *Joule* **2020**, *4* (8), 1688–1699. https://doi.org/10.1016/j.joule.2020.07.009.

(14) Irtem, E.; Arenas Esteban, D.; Duarte, M.; Choukroun, D.; Lee, S.; Ibáñez, M.; Bals, S.; Breugelmans, T. Ligand-Mode Directed Selectivity in Cu-Ag Core-Shell Based Gas Diffusion Electrodes for CO2Electroreduction. *ACS Catal* **2020**, *10* (22), 13468–13478. https://doi.org/10.1021/acscatal.0c03210.

(15) Lee, C.; Kim, N. R.; Koo, J.; Lee, Y. J.; Lee, H. M. Cu-Ag Core–Shell Nanoparticles with Enhanced Oxidation Stability for Printed Electronics. *Nanotechnology* **2015**, *26* (45), 455601. https://doi.org/10.1088/0957-4484/26/45/455601.

(16) Chang, Z.; Huo, S.; Zhang, W.; Fang, J.; Wang, H. The Tunable and Highly Selective Reduction Products on Ag@Cu Bimetallic Catalysts Toward CO_2 Electrochemical Reduction Reaction. *The*

Journal of Physical Chemistry C **2017**, *121* (21), 11368–11379. https://doi.org/10.1021/acs.jpcc.7b01586.

(17) Park, J.; Kwon, T.; Kim, J.; Jin, H.; Kim, H. Y.; Kim, B.; Joo, H.; Lee, K. Hollow Nanoparticles as Emerging Electrocatalysts for Renewable Energy Conversion Reactions. *Chem Soc Rev* **2018**. https://doi.org/10.1039/C8CS00336J.

(18) Su, D. Advanced Electron Microscopy Characterization of Nanomaterials for Catalysis. *Green Energy and Environment* **2017**, *2* (2), 70–83. https://doi.org/10.1016/j.gee.2017.02.001.

(19) *Electron Tomography*; Frank, J., Ed.; Springer US: Boston, MA, 1992. https://doi.org/10.1007/978-1-4757-2163-8.

(20) Midgley, P. A.; Bals, S. Electron Tomography. In *Handbook of Nanoscopy*; Wiley, 2012; pp 253–279. https://doi.org/10.1002/9783527641864.ch7.

(21) Jeklin, A. Au@Ag Nanoparticles: Halides Stabilize {100} Facets. *J Phys Chem Lett* **2016**, No. July, 1–23.

(22) Osowiecki, W. T.; Ye, X.; Satish, P.; Bustillo, K. C.; Clark, E. L.; Alivisatos, A. P. Tailoring Morphology of Cu–Ag Nanocrescents and Core–Shell Nanocrystals Guided by a Thermodynamic Model. *J Am Chem Soc* **2018**, *140* (27), 8569–8577. https://doi.org/10.1021/jacs.8b04558.

(23) Choukroun, D.; Pacquets, L.; Li, C.; Hoekx, S.; Arnouts, S.; Baert, K.; Hauffman, T.; Bals, S.; Breugelmans, T. Mapping Composition–Selectivity Relationships of Supported Sub-10 Nm Cu–Ag Nanocrystals for High-Rate CO_2 Electroreduction. *ACS Nano* **2021**, *15* (9), 14858–14872. https://doi.org/10.1021/acsnano.1c04943.

(24) Altantzis, T.; Lobato, I.; De Backer, A.; Béché, A.; Zhang, Y.; Basak, S.; Porcu, M.; Xu, Q.; Sánchez-Iglesias, A.; Liz-Marzán, L. M.; Van Tendeloo, G.; Van Aert, S.; Bals, S. Three-Dimensional Quantification of the Facet Evolution of Pt Nanoparticles in a Variable Gaseous Environment. *Nano Lett* **2019**, *19* (1), 477–481. https://doi.org/10.1021/acs.nanolett.8b04303.

(25) van Aarle, W.; Palenstijn, W. J.; De Beenhouwer, J.; Altantzis, T.; Bals, S.; Batenburg, K. J.; Sijbers, J. The ASTRA Toolbox: A Platform for Advanced Algorithm Development in Electron Tomography. *Ultramicroscopy* **2015**, *157* (2015), 35–47. https://doi.org/10.1016/j.ultramic.2015.05.002.

(26) van Aarle, W.; Palenstijn, W. J.; Cant, J.; Janssens, E.; Bleichrodt, F.; Dabravolski, A.; De Beenhouwer, J.; Joost Batenburg, K.; Sijbers, J. Fast and Flexible X-Ray Tomography Using the ASTRA Toolbox. *Opt Express* **2016**, *24* (22), 25129. https://doi.org/10.1364/oe.24.025129.

(27) Bortsova, G.; Dubost, F.; Hogeweg, L.; Katramados, I.; de Bruijne, M. Semi-Supervised Medical Image Segmentation via Learning Consistency Under Transformations; 2019; pp 810–818. https://doi.org/10.1007/978-3-030-32226-7_90.

(28) Iyengar, P.; Kolb, M. J.; Pankhurst, J. R.; Calle-Vallejo, F.; Buonsanti, R. Elucidating the Facet-Dependent Selectivity for CO_2 Electroreduction to Ethanol of Cu–Ag Tandem Catalysts. *ACS Catal* **2021**, *11* (8), 4456–4463. https://doi.org/10.1021/acscatal.1c00420.

(29) Toh, H. S.; Batchelor-McAuley, C.; Tschulik, K.; Uhlemann, M.; Crossley, A.; Compton, R. G. The Anodic Stripping Voltammetry of Nanoparticles: Electrochemical Evidence for the Surface Agglomeration of Silver Nanoparticles. *Nanoscale* **2013**, *5* (11), 4884. https://doi.org/10.1039/c3nr00898c.

(30) Jović, V. D.; Jović, B. M. Surface Reconstruction during the Adsorption/Desorption of OH-Species onto Cu(111) and Cu(100) in 0.1 M NaOH Solution. *Journal of the Serbian Chemical Society* **2002**, *67* (7), 531–546. https://doi.org/10.2298/JSC0207531J.

(31) Clark, E. L.; Hahn, C.; Jaramillo, T. F.; Bell, A. T. Electrochemical CO2 Reduction over Compressively Strained CuAg Surface Alloys with Enhanced Multi-Carbon Oxygenate Selectivity. *J Am Chem Soc* **2017**, *139* (44), 15848–15857. https://doi.org/10.1021/jacs.7b08607.

(32) Kavak, S.; Kadu, A. A.; Claes, N.; Sánchez-Iglesias, A.; Liz-Marzán, L. M.; Batenburg, K. J.; Bals, S. Quantitative 3D Investigation of Nanoparticle Assemblies by Volumetric Segmentation of Electron Tomography Data Sets. *The Journal of Physical Chemistry C* **2023**, *127* (20), 9725–9734. https://doi.org/10.1021/acs.jpcc.3c02017.

(33) Milek, T.; Zahn, D. Molecular Simulation of Ag Nanoparticle Nucleation from Solution: Redox-Reactions Direct the Evolution of Shape and Structure. *Nano Lett* **2014**, *14* (8), 4913–4917. https://doi.org/10.1021/nl502503t.

(34) Wilde, P.; O'Mara, P. B.; Junqueira, J. R. C.; Tarnev, T.; Benedetti, T. M.; Andronescu, C.; Chen, Y.-T.; Tilley, R. D.; Schuhmann, W.; Gooding, J. J. Is Cu Instability during the CO_2 Reduction Reaction Governed by the Applied Potential or the Local CO Concentration? *Chem Sci* **2021**, *12* (11), 4028–4033. https://doi.org/10.1039/D0SC05990K.

(35) Gunathunge, C. M.; Li, X.; Li, J.; Hicks, R. P.; Ovalle, V. J.; Waegele, M. M. Spectroscopic Observation of Reversible Surface Reconstruction of Copper Electrodes under CO2 Reduction. *Journal of Physical Chemistry C* **2017**, *121* (22), 12337–12344. https://doi.org/10.1021/acs.jpcc.7b03910.

(36) Li, H.; Wei, P.; Gao, D.; Wang, G. In Situ Raman Spectroscopy Studies for Electrochemical CO2 Reduction over Cu Catalysts. *Curr Opin Green Sustain Chem* **2022**, *34*, 100589. https://doi.org/10.1016/j.cogsc.2022.100589.

(37) Lee, S. H.; Lin, J. C.; Farmand, M.; Landers, A. T.; Feaster, J. T.; Avilés Acosta, J. E.; Beeman, J. W.; Ye, Y.; Yano, J.; Mehta, A.; Davis, R. C.; Jaramillo, T. F.; Hahn, C.; Drisdell, W. S. Oxidation State and Surface Reconstruction of Cu under CO2Reduction Conditions from in Situ X-Ray Characterization. *J Am Chem Soc* **2021**, *143* (2), 588–592. https://doi.org/10.1021/jacs.0c10017.

(38) Jeon, H. S.; Timosnenko, J.; Scholten, F.; Sinev, I.; Herzog, A.; Haase, F. T.; Cuenya, B. R. Operando Insight into the Correlation between the Structure and Composition of CuZn Nanoparticles and Their Selectivity for the Electrochemical CO2 Reduction. *J Am Chem Soc* **2019**, *141* (50), 19879–19887. https://doi.org/10.1021/jacs.9b10709.

(39) Huang, J.; Mensi, M.; Oveisi, E.; Mantella, V.; Buonsanti, R. Structural Sensitivities in Bimetallic Catalysts for Electrochemical CO_2 Reduction Revealed by Ag–Cu Nanodimers. *J Am Chem Soc* **2019**, *141* (6), 2490–2499. https://doi.org/10.1021/jacs.8b12381.

TOC Graphic